Nanoscale imaging of light-matter coupling inside metal-coated cavities with a pulsed electron beam

Moerland, Robert Jan; Weppelman, Gerward; Scotuzzi, Marijke; Hoogenboom, Jacob P.

DOI
10.1021/acs.nanolett.8b00546

Publication date
2018

Document Version
Final published version

Published in
Nano Letters: a journal dedicated to nanoscience and nanotechnology

NANO LETTERS
Cite This: Nano Lett. XXXX, XXX, XXX−XXX
Letter
pubs.acs.org/NanoLett

Nanoscale Imaging of Light-Matter Coupling Inside Metal-Coated Cavities with a Pulsed Electron Beam

Robert J. Moerland,* I. Gerward C. Weppelman, Marijke Scotuzzi, and Jacob P. Hoogenboom*

Department of Imaging Physics, Delft University of Technology, NL-2600 GA Delft, The Netherlands

Supporting Information

ABSTRACT: Many applications in (quantum) nanophotonics rely on controlling light-matter interaction through strong, nanoscale modification of the local density of states (LDOS). All-optical techniques probing emission dynamics in active media are commonly used to measure the LDOS and benchmark experimental performance against theoretical predictions. However, metal coatings needed to obtain strong LDOS modifications in, for instance, nanocavities, are incompatible with all-optical characterization. So far, no reliable method exists to validate theoretical predictions. Here, we use subnanosecond pulses of focused electrons to penetrate the metal and excite a buried active medium at precisely defined locations inside subwavelength resonant nanocavities. We reveal the spatial layout of the spontaneous-emission decay dynamics inside the cavities with deep-subwavelength detail, directly mapping the LDOS. We show that emission enhancement converts to inhibition despite an increased number of modes, emphasizing the critical role of optimal emitter location. Our approach yields fundamental insight in dynamics at deep-subwavelength scales for a wide range of nano-optical systems.

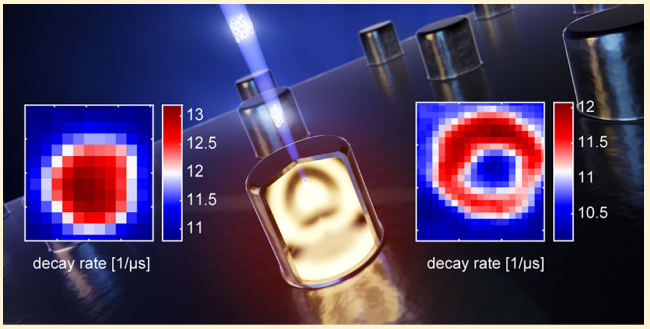

KEYWORDS: *Cathodoluminescence, decay dynamics, nanocavities, local density of states, electron microscopy*

Metallo-dielectric resonant nanocavities have been shown to be promising candidates for ultracompact lasers, keeping both the physical size of the resonator and the optical size of the mode small.[1−3] Spontaneous emission into modes other than the lasing mode increases the lasing threshold and causes additional noise in the output.[4,5] Therefore, control over the modes available for spontaneous emission, that is, the local density of states (LDOS),[6] is paramount. According to the Fermi Golden Rule, the emission decay rate γ of a single emitter, represented by a dipole, is proportional to the LDOS $\rho(\mathbf{r},\omega)$ in the direction of the dipole.[7,8] By structuring the nanoscale environment of the emitter, strong spatial modifications of the LDOS are made possible.

With subwavelength resonators, the variations in the LDOS are expected to be highly sensitive to the size of the cavity, as the amount of available modes is typically much lower than for macroscale lasers.[3] Therefore, the emergence of additional modes has a dramatic impact on the spatial dependence of light-matter coupling. However, assessing spatially resolved decay rates within the cavity, and thus the available modes and their coupling with the emitters, is impossible with optical far-field techniques due to the diffraction-limited spatial resolving power. Moreover, the optically opaque metal coating inhibits optical excitation, which therefore also rules out near-field optical techniques.[9−15] In passive plasmonic and dielectric structures, optical properties such as spectra and dispersion curves can be probed at subwavelength resolution using electron-beam spectroscopy.[8,16−22]

In this Letter, we use a pulsed electron beam and exploit the penetrating power of the focused electrons to directly resolve emission dynamics in buried active media inside metal-coated nanocavities (Figure 1a) with deep-subwavelength detail, mapping out the LDOS in space. We generate approximately 90 ps long bursts of electrons by blanking a continuous 4 kV electron beam (see also Section I in the Supporting Information).[23] This results in electron bunches with a typical penetration depth of about 40−100 nm into the dielectric in a volume of 4.4×10^{-4} μm^3 (see Section III of the Supporting Information). As a consequence, emitters (here, Ce^{3+}) inside the dielectric part (yttrium−aluminum garnet, YAG) of the cavity are locally excited and will emit photons at a rate that directly depends on the amount of modes available at each specific location, that is, the LDOS $\rho(\mathbf{r},\omega)$. Emitted photons are collected with an inverted light microscopy stage with a 60×, NA = 0.95 optical objective (Nikon) inside the SEM vacuum chamber (see Figure 1a and Section I of the Supporting Information).[24,25] The electron pulse length is much shorter than the typical decay rate of the emitters (70−80 ns), which allows us to use time-correlated single-photon counting to

Received: February 7, 2018
Revised: April 20, 2018
Published: April 26, 2018

DOI: 10.1021/acs.nanolett.8b00546
Nano Lett. XXXX, XXX, XXX−XXX

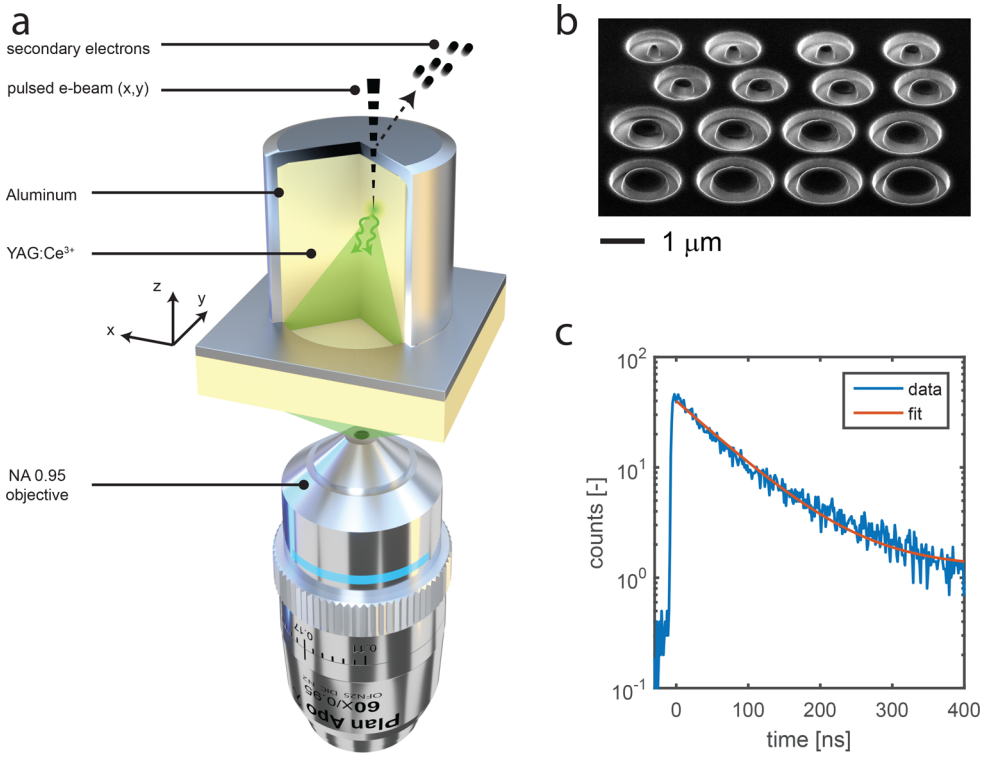

Figure 1. Probing dynamics inside metallo-dielectric cavities with deep-subwavelength resolution. (a) Shown is a cross section of a single nanocavity loaded with an active medium. A pulsed electron beam penetrates the top metal coating of a metallo-dielectric cavity at a user-defined location, exciting Ce^{3+} ions inside a YAG host. The rate of the resulting emission of photons is subject to the local density of states inside the cavity. Photons are collected at the bottom side of the sample without metal coating with a high-NA objective, placed directly in the vacuum chamber. (b) A SEM image of YAG pillars obtained through focused-ion-beam milling rings into a YAG substrate. The image is taken right after milling and before further post processing. (c) A typical example of photon arrival statistics of photons emitted by Ce^{3+} ions inside a metallo-dielectric cavity. A maximum-likelihood fit to the data with a single-exponential decay plus offset $\exp(-\gamma t) + C$ is used to approximate the decay curve. From the fit, the decay rate γ of the emitters is extracted.

record photon arrival histograms of the cerium emission.[26] Simultaneously, we collect the secondary electrons, thus obtaining surface topography and decay dynamics concurrently, with a resolution of about 50 nm.[23]

We fabricate nanoscale metallo-dielectric cavities by means of focused-ion-beam milling into a YAG substrate doped with Ce^{3+} ions (Crytur, 100 μm thickness). Before milling, the YAG substrate is coated with a 30 nm layer of chromium to prevent charging effects. Rings with various inner diameters are milled into the YAG wafer with a beam current of 26 pA at 30 kV. The outer diameter of the rings is maintained to be between 150−200 nm larger. This results in small pillars of YAG that are the dielectric load of the cavities (n = 1.83). A SEM image right after the milling is shown in Figure 1b, where the sample is tilted with respect to the electron-beam axis. The brighter area corresponds to the exposed YAG. Subsequently, we use a chromium etchant in order to remove the remaining chromium. Then, we perform an evaporation step where a layer of aluminum is coated onto the sample. The aluminum is the metal part of the cavity which strongly confines the light. Here, we use aluminum because of its high reflectance, chemical stability and bulk plasmon resonance frequency which lies deeply into the UV, which partially suppresses plasmonic effects relative to, e.g., silver. During the evaporation, the sample is tilted by 45° and rotates around its axis. This results in metal coverage on the top and sides of the cavity. The programmed thickness, as recorded by the crystal inside the evaporation chamber, is 60 nm.

Experiments were performed with a dwell time of 8 s per pixel with a pulse repetition rate of 1 MHz and a spatial step size of 25 nm. A typical photon arrival histogram is show in Figure 1c. Here, the photon arrival data is obtained while the electron beam repeatedly excites Ce^{3+} emitters at the same location inside a metallo-dielectric cavity. A well-known consequence of electronic stimulation of scintillator materials such as Ce^{3+}/YAG is the emergence of a slow decay component due to radiative energy transfer from longer-lived excitonic states.[27,28] Here, we concentrate on the main (fast) decay part of the curve, which could be considered the "primary" emission from the Ce^{3+}/YAG.[29] Therefore, we approximate the decay curve with a curve describing a single-exponential decay and background, $\exp(-\gamma t) + C$, where γ is the decay rate of the Ce^{3+} ions inside the cavity and C represents the background or offset due to the slow component. To obtain γ, we use a maximum-likelihood estimator and perform this procedure at every location inside each cavity and map γ versus the position in x and y. The results are collected in Figure 2. In the first column, we show a SEM image of the cavities as obtained by collecting the secondary electrons (SEs) generated by a continuous electron beam. The bottom-left corner states the programmed diameter of the YAG pillar. The second column contains the normalized SE signal, collected during pulsed operation. Because of drift, the concurrently obtained images are somewhat distorted compared to the SE images in the first column. Ellipses are fitted to the normalized SE signal in order to outline the circumference of the cavity in the third and

DOI: 10.1021/acs.nanolett.8b00546
Nano Lett. XXXX, XXX, XXX−XXX

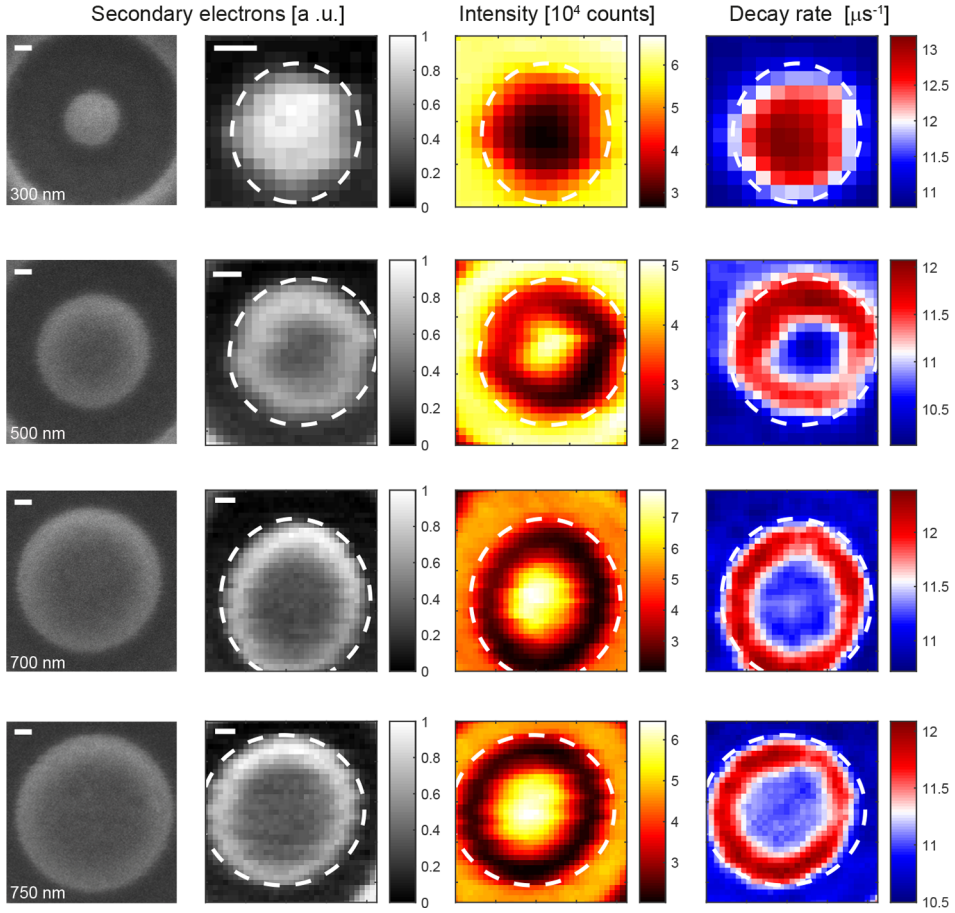

Figure 2. Decay dynamics inside metallo-dielectric cavities of increasing diameter. Column 1: secondary-electron (SE) image collected with a continuous electron beam. Programmed diameters of the YAG cylinders are shown in the bottom-left corner. Column 2: SE image collected with a pulsed electron beam. The ellipse is a fit to the SE image and reproduced in columns 3 and 4 to outline the circumference of the cavity. Column 3: Number of collected photons during pulsed operation, as a function of location. Column 4: decay rates as a function of location, based on a single-exponential fit of photon-arrival histograms. The scale bar is 100 nm in all figures.

fourth columns. The third column contains the number of photons, collected during the measurement as a function of location. The fourth column contains the decay rates that we measure, based on a single-exponential fit of the photon-arrival histograms as explained above. The decay rates are mildly spatially filtered with a Gaussian kernel (σ = 0.7 pixels).

As is visible in Figure 2, the decay rate of the Ce^{3+} ions in the medium, and therefore the coupling of Ce^{3+} with the LDOS, is strongly dependent on the position of the ions inside the cavity. Moreover, areas where initially the spontaneous emission was enhanced can convert to areas of inhibited emission as the size of the cavity changes. As an example, for the smallest cavity (300 nm), the strongest coupling to the available modes occurs at the center, and the coupling strength diminishes toward the boundary. In complete contrast, Ce^{3+} ions in the 500 nm wide cavity couple the least strongly to the available modes at the center, and the coupling strength increases toward the boundary. All-optical experiments would only yield the average decay rates of each cavity, which are the same within 8%. Moreover, the subwavelength spatial dependence of the light-matter interaction inside the nanocavities would go unnoticed entirely.

In Figure 3a, cross sections are shown of the experimentally obtained decay dynamics inside the cavities. For the cavity of 300 nm size, the decay rate has a maximum at the center and then decreases toward the edges. For a cavity size of 500 nm, a minimum develops at the center and a ring-shaped maximum is found at the outer edge of the cavity (red curve in Figure 3a). Further increasing the cavity size to 700 nm, a new peak in decay rate appears at the center but is smaller in amplitude than before. The emergence of a new maximum is conclusive proof that the decay rate and the collected intensities are not correlated, ruling out artifacts in the measurement. Finally, for the largest cavity, a minimum again is present at the center, which admittedly is at the limit of our detection sensitivity. The minimum is made more clear with the inset in Figure 3a.

To understand our observations and obtain insight into the underlying physics, we forego extensive numerical finite-element simulations and approximate the metallo-dielectric cavities by viewing them as circular cylindrical waveguides with a certain diameter, closed off by a perfect conductor on one end. This allows for a (semi)analytical treatment of the relative decay rate γ/γ_0 of a single emitter in such a structure by calculating the power P emitted by a classical dipole in the structure and the power P_0 emitted by the same dipole in homogeneous space filled with YAG. Then, with $\gamma/\gamma_0 = P/P_0$ the relative decay rate can be obtained.[30] We treat the Ce^{3+}-ions as an isotropic emitter and therefore determine the theoretical relative decay rate γ_{iso} of the emitter by averaging the decay rate of three orthogonal dipoles: $\gamma_{iso} = (\gamma_x + \gamma_y + \gamma_z)/(3\gamma_0)$.[31] See Section II and Figure S2 for the derivation of the analytical

DOI: 10.1021/acs.nanolett.8b00546
Nano Lett. XXXX, XXX, XXX−XXX

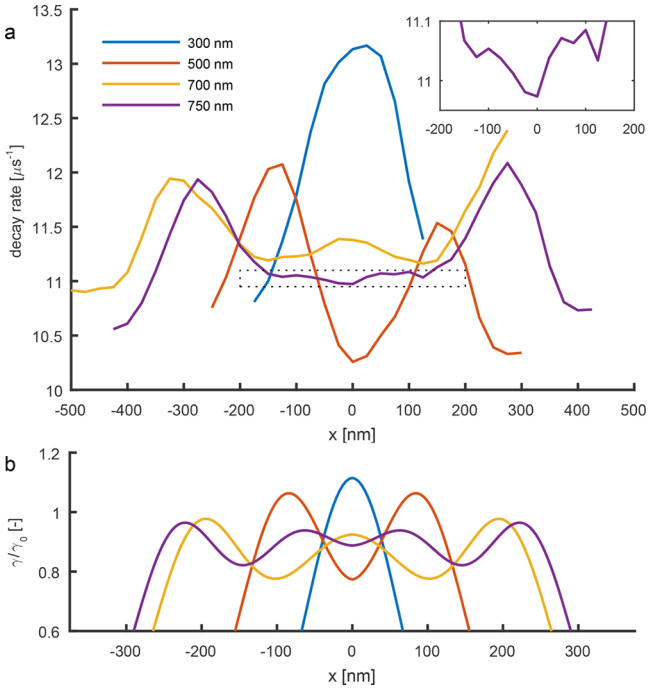

Figure 3. Cross sections of decay rates. (a) Cross sections of experimentally obtained decay rates (column 4 in Figure 2). For the cavity of 300 nm size (blue curve), the decay rate has a maximum at the center. For a cavity size of 500 nm (red curve), a minimum develops at the center and a ring-shaped maximum is found at the outer edge. For a cavity of 700 nm, a new peak in decay rate appears at the center. Finally, for the largest cavity of 750 nm, a minimum again is present at the center. The inset highlights the minimum for the largest cavity by expanding the *y*-axis of the part of the graph indicated by the dotted rectangle. (b) Cross sections of the calculated, isotropically averaged relative decay rates, corresponding to the cavities in (a), calculated with a semianalyical model (see Sections II and III of the Supporting Information). The trends in the experimental results agree well with the model predictions.

model for emission by a classical single dipole in a capped cylindrical waveguide.

Furthermore, in our experiment the electron interaction volume has a small but finite size due to the scattering of the highly energetic electrons inside the YAG. The free electron−hole pairs generated by the incoming electrons are responsible for the excitation of the Ce^{3+} ions in the YAG host.[28] Unfortunately, to analytically determine the exact rate of generation of electron−hole pairs by the incoming electrons is a nontrivial task, as multiple processes contribute to electron−hole pair generation.[32] Instead, as a first approximation, we use the (average) local energy loss profile of the scattered electrons and assume that a constant fraction of the energy is used to generate electron−hole pairs[32] inside the YAG and at a constant beam energy. As a consequence, Ce^{3+} emitters are excited throughout the interaction volume with a rate that is proportional to the electron energy loss profile. We estimate the electron interaction volume through Monte Carlo simulation[33] and collect the scattering traces of 10^5 electrons. For each scatter event, the energy loss is recorded with the position and used to build a three-dimensional energy-loss-based point spread function (PSF). See Section III in the Supporting Information for details on the Monte Carlo simulations and Figure S3 for a plot of the electron scattering density and energy loss-based PFSs, where the scattering events and energy loss have been discretized on a 5 × 5 × 5 nm grid.

With $E_{loss}(\mathbf{r})$ the energy loss-based PSF and $\mathbf{r} = (x,y,z)$ a vector iterating over all grid points of the PSF, we can calculate the expected average relative decay rate $\hat{\gamma}_{iso}(\mathbf{r}_0)$, for any point of entry of the electron beam $\mathbf{r}_0 = (x_0,y_0)$ in the *xy*-plane. We first calculate $\gamma_{iso}(\mathbf{r} + \mathbf{r}_0)$ at every grid point inside a volume the size of $E_{loss}(\mathbf{r})$, where we iterate over $\mathbf{r}$. Then, we sum the decay rates where weighting with the PSF is applied, which yields an average relative decay rate for the volume and location probed by the electron beam: $\hat{\gamma}_{iso}(\mathbf{r}_0) = [\sum_{\mathbf{r}}\gamma_{iso}(\mathbf{r} + \mathbf{r}_0)E_{loss}(\mathbf{r})]/\sum_{\mathbf{r}}E_{loss}(\mathbf{r})$. In doing so, we treat the dipoles as isolated emitters, that is, we assume that effects such as super radiance,[34] strong coupling,[35] dipole−dipole energy transfer[36] and amplified spontaneous emission or lasing[1−3] are negligible. This is a very reasonable approximation as the concentration of the Ce^{3+} ions is less than 0.35 at. % and the decay rate modifications (i.e., Purcell factors) inside the cavities are moderate. By stepping the coordinates in the *xy*-plane, we can calculate the theoretically expected relative decay rate over a cross section of the cavity. For the results we present here, the acceleration voltage of the electron beam was kept constant at 4 kV, leading to an average of the depth-dependent decay rate. In general, the acceleration voltage may be varied in order to also probe the depth-dependence of the decay rate in nanophotonic structures, see also Section IV.

The results of the semianalytical treatment are shown in Figure 3b. In general, the decay rates obtained through this semianalytical method are qualitatively in agreement with the measurements. We attribute the differences to the fact that our cavities are coated with aluminum, which is not a perfect conductor. This influences the decay rate in various ways: the first is that plasmon effects, which may occur particularly close to cavity walls,[37,38] are ignored in our model. Furthermore, quenching of radiation through energy transfer to the absorbing metal coating may occur.[39] Both these phenomena result in a higher decay rate close to the metal than what would be expected based on a coating with a perfect conductor. However, in order to estimate the order of magnitude of nonradiative pathways, we perform a set of fully three-dimensional finite-element simulations. We restrict ourselves to the smallest structure, which is a worst-case scenario since the metallic walls are closest to the emitters and the moderate decay rate modifications exclude strongly resonantly enhanced losses. The details of this simulation are presented in Section V in the Supporting Information. From these simulations, we estimate the fraction of nonradiative pathways in our structures to be typically about 35%−40% for depths that are probed by the electron beam, with the exception of emitters which are very close (<30 nm) to the aluminum walls (side or top). There, the fraction of nonradiative pathways rises quickly to 100% due to nonradiative energy transfer to the metal. However, these losses to the metal may be reduced by, for example, adding dielectric shielding around the active medium.[2]

Continuing the discussion on the observed differences between our analytical model and the experiments, we further note that the reflection efficiency at the cavity walls is less than 100%, which therefore results in lower Q-factors. Also, our theoretical model assumes that the quantum yield of Ce^{3+} is unity, whereas values stated in literature are somewhat smaller for photoexcitation of Ce^{3+} in YAG.[40] Finally, the radial asymmetry in our experimental results indicate that the cavities might have some defects, for example, a locally thinner layer of

DOI: 10.1021/acs.nanolett.8b00546
Nano Lett. XXXX, XXX, XXX−XXX

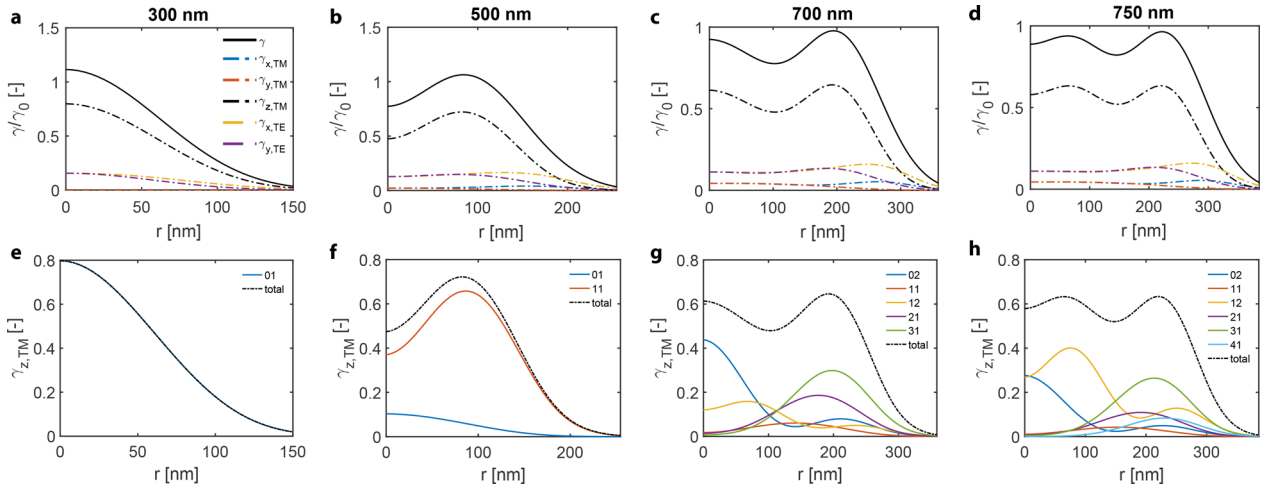

Figure 4. Coupling of isotropic dipoles to cavity modes. (a–d) Coupling of dipoles to TE and TM modes for the cavities designed to be 300, 500, 700, and 750 nm. The profile takes the three-dimensional electron interaction volume, obtained through a Monte Carlo simulation, into account. The modification of the spontaneous decay rate is dominated by TM modes, excited in the *z*-direction. (e–h) We identify the TM modes, based on our model, that are responsible for the oscillatory decay rate modification. Here, the graphs (e–h) correspond with (a–d), respectively. Furthermore, in (e–h) only those modes that are at least 5% part of the LDOS are shown. In (e), only the TM_{01} mode is above cutoff. For the 500 nm cavity the TM_{11} mode is essentially responsible for the spatial variation of the decay rate. In (g,h), the available modes are essentially identical but the strong presence of the TM_{12} mode in (h) drastically changes the spatial behavior.

aluminum. However, this underlines how well our approach can resolve such subtle issues that cannot be resolved otherwise.

The analytical model that we employ allows us to identify, up to a certain extent, the origins of the coupling of the emitters to modes inside the nanocavity. In Figure 4a–d, we show how the coupling to TE and TM modes by dipoles in the *x*, *y*, and *z* direction contributes to the total decay rate. The coupling to TM modes by *z*-oriented dipoles clearly dominates the total decay rate. TE modes are largely suppressed, as these only have electric fields parallel to the perfectly conducting end-cap, which must be zero at that location. Thus, optimal coupling is achieved by aligning dipole orientation in the cavity in the *z*-direction. In Figure 4e–h, we further resolved the TM modes excited by *z*-oriented dipoles and determine which TM modes the emitters couple to. For the smallest cavity (300 nm, Figure 4e), the only TM mode above cutoff is the TM_{01} mode. For the 500 nm cavity there are two competing modes (Figure 4f). The coupling to a dominant TM_{11} mode is responsible for essentially all spatial variations in the decay rate, since the coupling to the TM_{01} mode is negligible. For the remaining two cavities, there are 3–4 dominant modes; the major difference is the sudden jump in the coupling strength to the TM_{12} mode in the largest cavity (Figure 4g and 4h). This underlines the importance of fabricating nanoscale cavities with low tolerances, as perceptually small differences can have a strongly different modal behavior as a result.

We obtained the spatially dependent decay dynamics of emitters buried inside subwavelength resonant nanocavities through the use of time-resolved cathodoluminescence with a pulsed electron beam. We resolve the decay dynamics by employing time-correlated single-photon counting techniques, and as such obtain a map of the isotropically averaged LDOS inside these cavities. We demonstrate that a small change in cavity size can have large consequences considering optimal coupling of the emitter to the cavity. While here we employ a single acceleration voltage, leading to a fixed electron energy loss distribution in depth, it may be possible in future work to perform tomography, that is, resolve the LDOS as a function of depth by employing multiple acceleration voltages. This approach results into different depth distributions of the electron energy loss function which is the base of earlier tomographic work with electrons in a scanning electron microscope.[41] Our work demonstrates that time-resolved cathodoluminescence is a powerful technique to reveal the local decay dynamics and the density of states in nanophotonic structures with (buried) active media.

■ ASSOCIATED CONTENT

Supporting Information

The Supporting Information is available free of charge on the ACS Publications website at DOI: 10.1021/acs.nanolett.8b00546.

Details on the experimental setup, the derivation of the analytical model of a nanocavity, the estimate of the cathodoluminescence point-spread function, the depth dependence of the decay rate, and an estimate of the magnitude of nonradiative pathways in our system (PDF)

■ AUTHOR INFORMATION

Corresponding Authors

*E-mail: r.j.moerland@tudelft.nl.
*E-mail: j.p.hoogenboom@tudelft.nl.

ORCID

Robert J. Moerland: 0000-0003-2535-9047

Author Contributions

RJM performed the measurements, analyzed the data and performed the theoretical calculations and simulations. IGCW contributed to implementing time-resolved cathodoluminescence. MS and IGCW fabricated the sample. RJM and JPH conceived the experiment, discussed the data, and wrote the manuscript. JPH supervised the project. All authors have read and agreed with the contents of the manuscript.

DOI: 10.1021/acs.nanolett.8b00546
Nano Lett. XXXX, XXX, XXX–XXX

Notes

The authors declare the following competing financial interest(s): Our integrated microscope and cathodoluminescence detection set-up served as a prototype for a product by Delmic BV. JPH is co-founder and shareholder in Delmic.

■ ACKNOWLEDGMENTS

The authors thank C. Heerkens and M. Kamerbeek for performing additional sample fabrication steps and D. Brinks for a critical reading of the manuscript. This work was supported by The Netherlands Organization for Fundamental Research (NWO) and Foundation for Fundamental Research on Matter (10PR2826). M.S. acknowledges support from the European Union (Agreement No. 318804 - SNM; Single Nanometer Maufacturing for Beyond CMOS devices).

■ REFERENCES

(1) Hill, M. T.; Oei, Y.-S.; Smalbrugge, B.; Zhu, Y.; de Vries, T.; van Veldhoven, P. J.; van Otten, F. W. M.; Eijkemans, T. J.; Turkiewicz, J. P.; de Waardt, H.; Geluk, E. J.; Kwon, S.-H.; Lee, Y.-H.; Nötzel, R.; Smit, M. K. *Nat. Photonics* **2007**, *1*, 589−594.
(2) Nezhad, M. P.; Simic, A.; Bondarenko, O.; Slutsky, B.; Mizrahi, A.; Feng, L.; Lomakin, V.; Fainman, Y. *Nat. Photonics* **2010**, *4*, 395−399.
(3) Khajavikhan, M.; Simic, A.; Katz, M.; Lee, J. H.; Slutsky, B.; Mizrahi, A.; Lomakin, V.; Fainman, Y. *Nature* **2012**, *482*, 204−207.
(4) Siegman, A. *Lasers*; University Science Books, 1986.
(5) Noda, S.; Fujita, M.; Asano, T. *Nat. Photonics* **2007**, *1*, 449−458.
(6) Purcell, E. *Phys. Rev.* **1946**, *69*, 681.
(7) Grynberg, G.; Aspect, A.; Fabre, C. *Introduction to Quantum Optics: From the Semi-classical Approach to Quantized Light*; Cambridge University Press: Cambridge, 2010.
(8) Carminati, R.; Cazé, A.; Cao, D.; Peragut, F.; Krachmalnicoff, V.; Pierrat, R.; De Wilde, Y. *Surf. Sci. Rep.* **2015**, *70*, 1−41.
(9) Michaelis, J.; Hettich, C.; Mlynek, J.; Sandoghdar, V. *Nature* **2000**, *405*, 325.
(10) Kühn, S.; Hettich, C.; Schmitt, C.; Poizat, J. P.; Sandoghdar, V. *J. Microsc.* **2001**, *202*, 2−6.
(11) Hoogenboom, J. P.; Sanchez-Mosteiro, G.; Colas des Francs, G.; Heinis, D.; Legay, G.; Dereux, A.; van Hulst, N. F. *Nano Lett.* **2009**, *9*, 1189−95.
(12) Frimmer, M.; Chen, Y.; Koenderink, A. F. *Phys. Rev. Lett.* **2011**, *107*, 123602.
(13) Schell, A. W.; Engel, P.; Werra, J. F. M.; Wolff, C.; Busch, K.; Benson, O. *Nano Lett.* **2014**, *14*, 2623−2627.
(14) Cao, D.; Cazé, A.; Calabrese, M.; Pierrat, R.; Bardou, N.; Collin, S.; Carminati, R.; Krachmalnicoff, V.; De Wilde, Y. *ACS Photonics* **2015**, *2*, 189−193.
(15) Guo, K.; Verschuuren, M. A.; Koenderink, A. F. *Optica* **2016**, *3*, 289−298.
(16) Kuttge, M.; Vesseur, E. J. R.; Koenderink, A. F.; Lezec, H. J.; Atwater, H. A.; García de Abajo, F. J.; Polman, A. *Phys. Rev. B: Condens. Matter Mater. Phys.* **2009**, *79*, 113405.
(17) Suzuki, T.; Yamamoto, N. *Opt. Express* **2009**, *17*, 23664−23671.
(18) García de Abajo, F. *Rev. Mod. Phys.* **2010**, *82*, 209−275.
(19) Takeuchi, K.; Yamamoto, N. *Opt. Express* **2011**, *19*, 12365−74.
(20) Coenen, T.; Vesseur, E. J.; Polman, A. *ACS Nano* **2012**, *6*, 1742−50.
(21) Sapienza, R.; Coenen, T.; Renger, J.; Kuttge, M.; van Hulst, N. F.; Polman, A. *Nat. Mater.* **2012**, *11*, 781−7.
(22) Kociak, M.; Stephan, O. *Chem. Soc. Rev.* **2014**, *43*, 3865−3883.
(23) Moerland, R. J.; Weppelman, I. G. C.; Garming, M. W. H.; Kruit, P.; Hoogenboom, J. P. *Opt. Express* **2016**, *24*, 24760−24772.
(24) Zonnevylle, A. C.; Van Tol, R. F.; Liv, N.; Narváez, A. C.; Effting, A. P.; Kruit, P.; Hoogenboom, J. P. *J. Microsc.* **2013**, *252*, 58−70.
(25) Narváez, A. C.; Weppelman, I. G.; Moerland, R. J.; Liv, N.; Zonnevylle, A. C.; Kruit, P.; Hoogenboom, J. P. *Opt. Express* **2013**, *21*, 29968−78.
(26) Garming, M. W. H.; Weppelman, I. G. C.; de Boer, P.; Martinez, F. P.; Schirhagl, R.; Hoogenboom, J. P.; Moerland, R. J. *Nanoscale* **2017**, *9*, 12727−12734.
(27) Leo, W. R. *Techniques for nuclear and particle physics experiments: a how-to approach*, 1st ed.; Springer-Verlag, 1987.
(28) Zych, E.; Brecher, C.; Glodo, J. *J. Phys.: Condens. Matter* **2000**, *12*, 1947−1958.
(29) Ludziejewski, T.; Moszyński, M.; Kapusta, M.; Wolski, D.; Klamra, W.; Moszyńska, K. *Nucl. Instrum. Methods Phys. Res., Sect. A* **1997**, *398*, 287−294.
(30) Novotny, L.; Hecht, B. *Principles of Nano-Optics*, 1st ed.; Cambridge University Press: Cambridge, 2006.
(31) Barnes, W. L. *J. Mod. Opt.* **1998**, *45*, 661−699.
(32) Toth, M.; Phillips, M. R. *Scanning* **1998**, *20*, 425−432.
(33) Hovington, P.; Drouin, D.; Gauvin, R. *Scanning* **1997**, *19*, 1−14.
(34) Dicke, R. H. *Phys. Rev.* **1954**, *93*, 99−110.
(35) Raizen, M. G.; Thompson, R. J.; Brecha, R. J.; Kimble, H. J.; Carmichael, H. J. *Phys. Rev. Lett.* **1989**, *63*, 240−243.
(36) Barnett, S. M.; Huttner, B.; Loudon, R.; Matloob, R. *J. Phys. B: At., Mol. Opt. Phys.* **1996**, *29*, 3763.
(37) Drexhage, K. H. *J. Lumin.* **1970**, *1−2*, 693−701.
(38) Chance, R. R.; Miller, A. H.; Prock, A.; Silbey, R. *J. Chem. Phys.* **1975**, *63*, 1589.
(39) Pockrand, I.; Brillante, A.; Möbius, D. *Chem. Phys. Lett.* **1980**, *69*, 499−504.
(40) Gorrotxategi, P.; Consonni, M.; Gasse, A. *J. Solid State Light.* **2015**, *2*, 1.
(41) Boughorbel, F.; Zhuge, X.; Potocek, P.; Lich, B. *Microsc. Microanal.* **2012**, *18*, 560−561.

DOI: 10.1021/acs.nanolett.8b00546
Nano Lett. XXXX, XXX, XXX−XXX